Structure of ATP synthase under strain during catalysis

Hui Guo [1,2] & John L. Rubinstein [1,2,3 ✉]

ATP synthases are macromolecular machines consisting of an ATP-hydrolysis-driven F_1 motor and a proton-translocation-driven F_O motor. The F_1 and F_O motors oppose each other's action on a shared rotor subcomplex and are held stationary relative to each other by a peripheral stalk. Structures of resting mitochondrial ATP synthases revealed a left-handed curvature of the peripheral stalk even though rotation of the rotor, driven by either ATP hydrolysis in F_1 or proton translocation through F_O, would apply a right-handed bending force to the stalk. We used cryoEM to image yeast mitochondrial ATP synthase under strain during ATP-hydrolysis-driven rotary catalysis, revealing a large deformation of the peripheral stalk. The structures show how the peripheral stalk opposes the bending force and suggests that during ATP synthesis proton translocation causes accumulation of strain in the stalk, which relaxes by driving the relative rotation of the rotor through six sub-steps within F_1, leading to catalysis.

[1] Molecular Medicine Program, The Hospital for Sick Children, Toronto, Ontario, Canada. [2] Department of Medical Biophysics, The University of Toronto, Toronto, Ontario, Canada. [3] Department of Biochemistry, The University of Toronto, Toronto, Ontario, Canada. ✉email: john.rubinstein@utoronto.ca

TP synthases use a transmembrane electrochemical proton motive force (pmf) to generate adenosine triphosphate (ATP) from adenosine diphosphate (ADP) and inorganic phosphate (Pi). The enzyme complex consists of two molecular motors positioned to oppose each other's action on a shared rotor subcomplex (Fig. 1a, left). The membrane-embedded F_O motor is driven by proton translocation across the membrane through two offset half channels[1,2] while the soluble F_1 motor is powered by ATP hydrolysis. In *Saccharomyces cerevisiae*, the F_O region contains subunits a, e, f, g, i/j, k, 8, part of subunit b, and the c_{10}-ring of the rotor[3], while the F_1 region includes a trimer of catalytic subunit αβ pairs and subunits γ, δ, and ε from the rotor[4]. Coupling between F_1 and F_O requires that the two motors are held stationary relative to each other by a peripheral stalk subcomplex (Fig. 1a, green structure), which in yeast is formed from subunits b, d, h, and OSCP (the oligomycin sensitivity conferral protein).

During ATP synthesis, proton translocation through F_O at the interface of subunit a and the c-ring causes the $γδεc_{10}$ rotor (Fig. 1a, outlined in black) to turn. Rotation of subunit γ within F_1 leads each αβ pairs to cycle through open, tight, and loose conformations that result in the formation of ATP. Conversely, sequential ATP hydrolysis at each of the three αβ pairs in F_1 causes the γ subunit to turn in the opposite direction, rotating the proton-carrying c-ring against subunit a in F_O and pumping protons across the membrane. Even with the rotor turning at hundreds of revolutions per second[5,6] there is little or no 'slip'[7] and the H^+:ATP ratio remains constant. In *S. cerevisiae* this ratio is 10:3 due to the ten proton-carrying c subunits in F_O and three catalytic sites in F_1[8]. With this H^+:ATP ratio, when 10× the free energy of proton translocation ($\triangle\widetilde{\mu}_{H^+}$) is more negative than 3× the free energy of ATP hydrolysis ($\triangle G_{ATP}$) the F_O motor overpowers the F_1 motor, forcing it to synthesize ATP. When
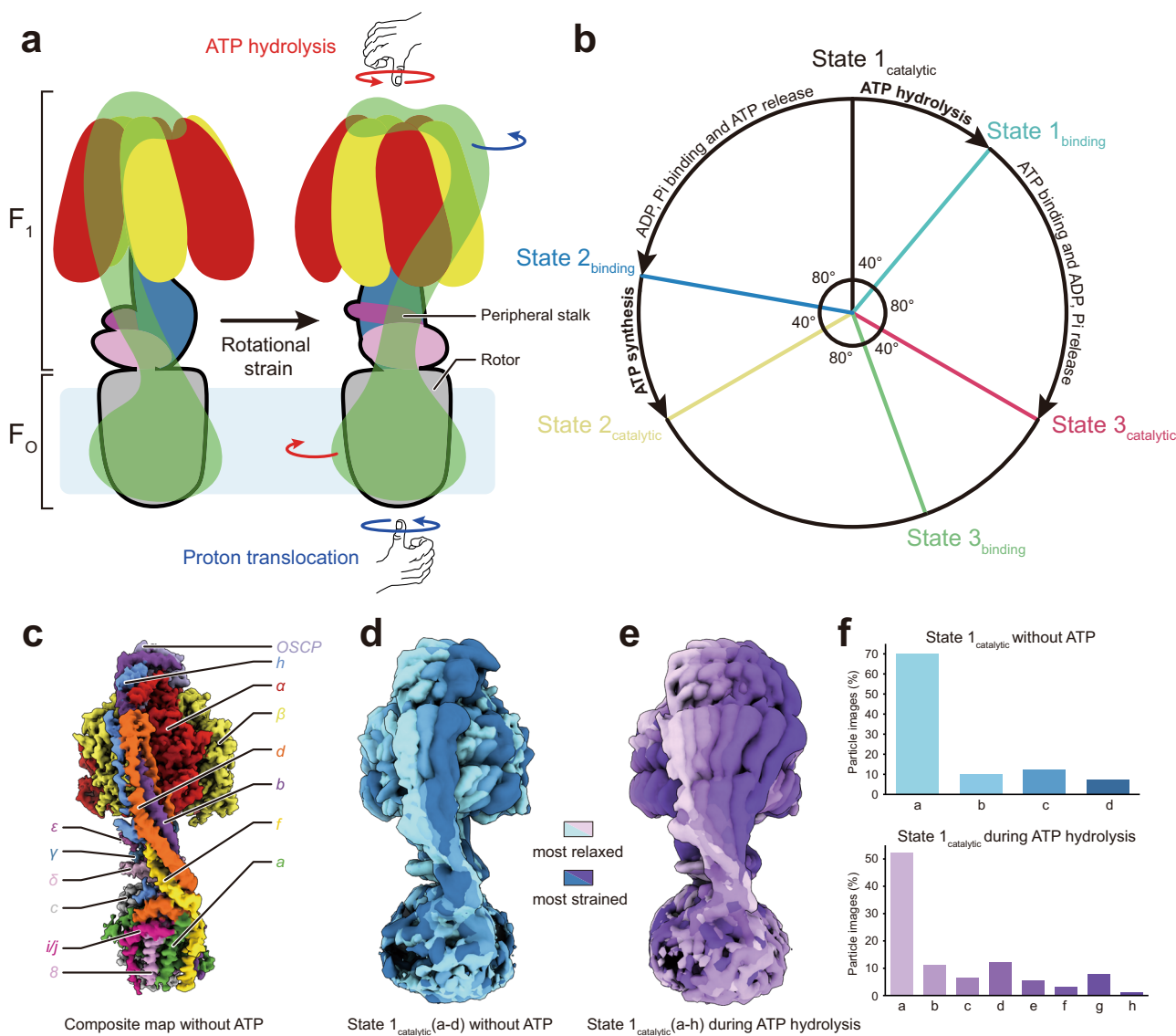

Fig. 1 Rotation in ATP synthase. a ATP synthase (left) consists of an F_1 and an F_O region with a shared rotor subcomplex (outlined in black) and a peripheral stalk (green). Rotation driven by proton translocation through the F_O region, or the opposite rotation driven by ATP hydrolysis in the F_1 region, are predicted to induce a right-handed bend of the peripheral stalk (right). **b** ATP hydrolysis or synthesis in the F_1 region requires three catalytic (black, yellow, and red) and three bind dwell (light blue, blue, and green) conformations. **c** High-resolution structure of the yeast mitochondrial ATP synthase. **d** In the absence of free ATP, the peripheral stalk exhibits limited flexibility with a left-handed curvature. **e** During ATP hydrolysis, ATP synthase can adopt conformations that show a right-handed curvature of the peripheral stalk. **f** Histograms of the distribution of conformations in the absence of ATP (top, blue) and during ATP hydrolysis (bottom, purple).

$3 \times \triangle G_{ATP}$ is more negative than $10 \times \triangle \widetilde{\mu}_{H^+}$, F_1 overpowers F_O and the enzyme hydrolyzes ATP to pump protons.

Synthesis or hydrolysis of each ATP molecule is associated with a ~120° rotation of the γ subunit within F_1, leading to conformations of the enzyme known as rotational State 1, 2, and 3 Ref. [9]. During ATP hydrolysis, which is better studied than ATP synthesis, this ~120° rotation is broken down into a ~40° sub-step as the enzyme transitions from a 'catalytic dwell' to a 'binding dwell', and an ~80° sub-step as the enzyme transitions to the next catalytic dwell[5,10–12] (Fig. 1b, clockwise). ATP hydrolysis likely occurs during the ~40° sub-step while ATP binding likely occurs during the ~80° sub-step[12–14]. Consequently, the expected sequence of states for a 360° rotation of the rotor during ATP synthesis is State $1_{binding}$ → State $1_{catalytic}$ → State $2_{binding}$ → State $2_{catalytic}$ → State $3_{binding}$ → State $3_{catalytic}$ (Fig. 1b, counter-clockwise). The mismatch between these six sub-steps in F_1 and the ten proton-translocation steps in F_O suggests that the enzyme cycles between strained and relaxed conformations during catalysis[15,16]. Early cryoEM noted that the peripheral stalks of mitochondrial ATP synthases have a left-handed curvature[17,18] (Fig. 1a, left). However, torque applied to the rotor following proton translocation through F_O (Fig. 1a, right, blue arrows) would tend to rotate the $\alpha_3\beta_3$ hexamer in the same direction as the torque, inducing a right-handed curvature of the peripheral stalk as it resists the rotation. Similarly, the opposite torque applied to the opposite end of the rotor by ATP hydrolysis in F_1 (Fig. 1a, right, red arrows) would tend to rotate the membrane-embedded region of F_O along with the c-ring, also inducing a right-handed curvature of the peripheral stalk as it resists the rotation[17]. Previously observed structures were obtained in the absence of a pmf or free ATP[9,17–30], suggesting that the peripheral stalk may act as a spring that has a left-handed curvature when relaxed but a right-handed curvature under strain during catalysis[17].

Results and discussion

The peripheral stalk shows pronounced bending under strain during ATP hydrolysis. We purified *S. cerevisiae* ATP synthase with the detergent n-Dodecyl-β-D-Maltopyranoside (DDM), which results in a monomeric preparation of the enzyme[30,31], and determined its structure by cryoEM (Supplementary Figs. 1 and 2, Supplementary Tables 1 and 2). A high-resolution map of the intact complex was generated by combining multiple maps from focused refinements (Fig. 1c and Supplementary Fig. 1c). In this map, the peripheral stalk shows the left-handed curvature seen previously. Three-dimensional (3D) classification allowed particle images to be separated into six rotor positions, corresponding to the catalytic and binding dwells for each of the three main rotational states. These conformations resemble recent catalytic and binding dwell structures for an isolated bacterial F_1 subcomplex imaged during ATP hydrolysis, where the absence of the peripheral stalk resulted in all catalytic dwell structures being identical and all binding dwell structures being identical[32]. For yeast ATP synthase imaged without ATP, the catalytic dwell structures show $\alpha\beta_{tight}$ either in the open conformation lacking nucleotide or in a closed conformation with weak nucleotide density, and the binding dwell structures show $\alpha\beta_{tight}$ only in an open conformation without nucleotide (Supplementary Fig. 3). The existence of $\alpha\beta_{tight}$ in an open conformation without visible nucleotide density is likely an artifact from loss of ATP during the purification of the enzyme. Further classification of the State $1_{catalytic}$ conformation resulted in classes distinguished by variability in the position of the peripheral stalk and a slight rotation of the rotor relative to subunit a. These classes were designated as State $1_{catalytic}$(a) (Fig. 1d, light blue) to State $1_{catalytic}$(d) (Fig. 1d, dark blue) in order of increasing straightening of the peripheral

stalk (Supplementary Movie 1, 'no ATP' condition). As these structures were determined in the absence of free ATP, they likely represent energetically similar conformations that can be reached by thermal fluctuation of the enzyme structure[9,26].

To test the hypothesis that the peripheral stalk of ATP synthase deforms under strain, we next added ATP to the preparation and froze cryoEM specimens. The presence of ATP in the cryoEM sample buffer introduces a concentration-dependant background noise and loss of contrast in images of DDM-solubilized ATP synthase (Supplementary Fig. 5A). Therefore, a delicate balance is required to provide sufficient ATP in solution to ensure that the enzyme is active as grids are frozen, while simultaneously maintaining sufficient contrast and image quality for image analysis. Initially, a small dataset of images was collected with a screening electron microscope where 10 mM ATP was added to the preparation at 4 °C and cryoEM specimens were frozen within 10 s. Analysis of this dataset revealed conformations of the enzyme not seen in the absence of free ATP (Supplementary Fig. 4). Therefore, a large dataset was collected for the specimen with a high-resolution microscope (Supplementary Fig. 5). Classification of the resulting dataset yielded maps showing six different F_1 states, corresponding to the catalytic and binding dwell structures from each of the three main rotational states. Subclassification of these populations separated each catalytic and each binding state into conformations with increasing rotation of the rotor relative to subunit a, and increasingly strained peripheral stalks, designated as 'a', 'b', 'c', etc. Overall, 27 unique conformations were identified: State $1_{binding}$(a to d), State $1_{catalytic}$(a to h), State $2_{binding}$(a to b), State $2_{catalytic}$(a to e), State $3_{binding}$(a to c), and State $3_{catalytic}$(a to e). Overlaying the eight State $1_{catalytic}$(a to h) structures reveals that during ATP hydrolysis the peripheral stalk exhibits a large bending motion, transitioning from a left-handed curvature (Fig. 1e, light purple) to the predicted right-handed curvature (Fig. 1e, dark purple; Supplementary Movie 1, 'During ATP hydrolysis' condition). Without ATP and during ATP hydrolysis, the left-handed curvature of the peripheral stalk remains the most highly populated conformation of the enzyme (Fig. 1f).

The flexible peripheral stalk accommodates rigid rotation of the rotor during ATP hydrolysis. To facilitate comparison of the ATP synthase conformations that occur during ATP hydrolysis, backbone models of the protein structure were fit flexibly into each of the 27 maps (Fig. 2a). Remarkably, the $\alpha_3\beta_3\gamma\delta\epsilon c_{10}$ models from all 18 catalytic dwell conformations could be overlaid with high-fidelity (Fig. 2b, left), as could the nine $\alpha_3\beta_3\gamma\delta\epsilon c_{10}$ models from binding dwell conformations (Fig. 2b, right), with some limited flexibility at the interface between F_1 and the c-ring. This observation shows that, other than being in a catalytic or binding dwell conformation, the differences between the structures are mostly due to deformation of the peripheral stalk subunits and the rotation of the c-ring relative to subunit a in F_O. Comparison of the eight State $1_{catalytic}$ models shows that the $\alpha_3\beta_3\gamma\delta\epsilon c_{10}$ rotor can turn ~80° against subunit a in F_O, or more than one-fifth of a complete revolution, before transition to the next binding dwell conformation (Fig. 2c). Bending of the peripheral stalk and not the central rotor of the complex supports suggestions that the peripheral stalk is the most compliant part of the enzyme and stores energy during rotary catalysis[9,21,22,26,28,33,34].

The peripheral stalk bends by deformation of subunits d, f, and h. The peripheral stalk of yeast ATP synthase contains subunits b, d, h, and OSCP (Fig. 3a). Although atomic models for subunits b, d, and OSCP have been constructed from previous cryoEM of ATP synthase[30], model quality for the 92-residue subunit h in
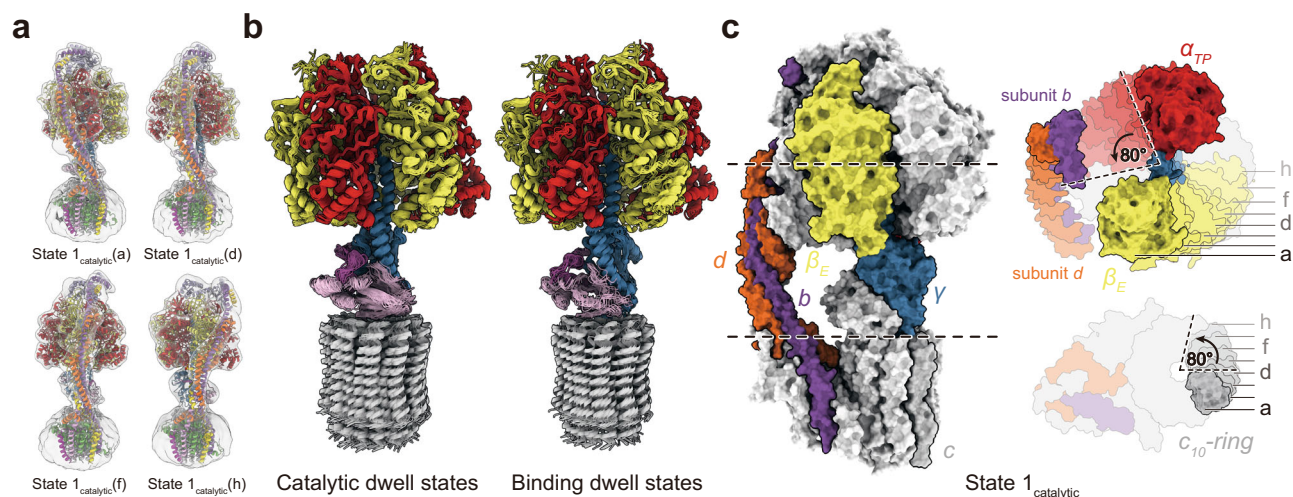
Fig. 2 Atomic models of ATP synthase under strain during ATP hydrolysis. a Atomic models of the enzyme were generated by flexible fitting of the atomic models of ATP synthase without ATP into maps of the strained ATP synthase conformations. **b** Overlay of fitted models from catalytic dwell (left) and binding dwell (right) structures show limited conformational changes in the $\alpha_3\beta_3\gamma\delta\epsilon c_{10}$ subcomplex. **c** Overlay of models from catalytic dwell conformations show pronounced bending of the peripheral stalk while the enzyme is under strain during ATP hydrolysis.
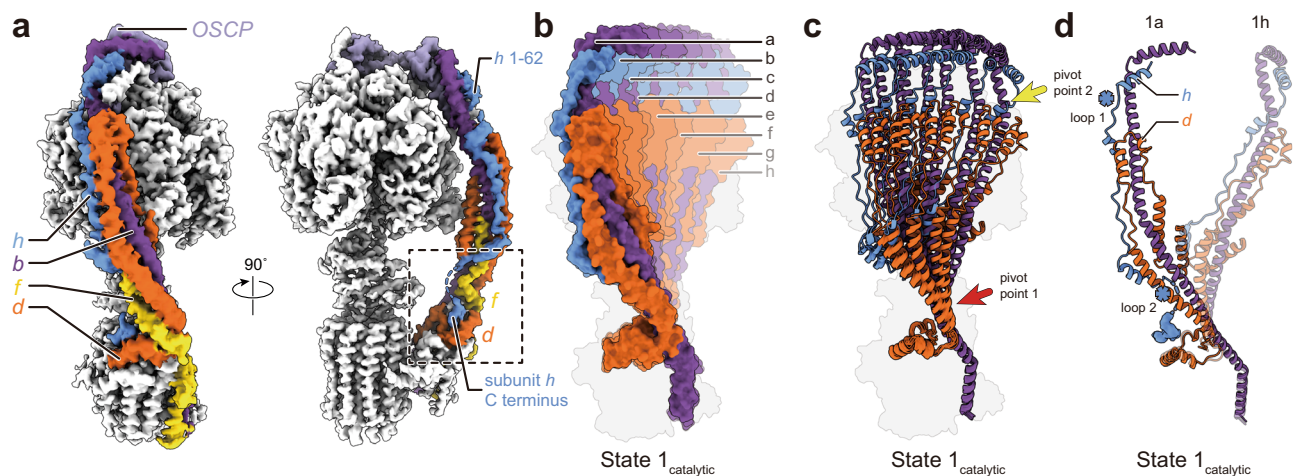

Fig. 3 Deformation of the peripheral stalk of ATP synthase while under strain during ATP hydrolysis. a Structure of the peripheral stalk shows that subunit h bridges F_1 and F_O. **b** Overlay of the eight State $1_{catalytic}$ atomic models, produced by molecular dynamics flexible fitting of the atomic model of resting ATP synthase into the eight 3D maps of State $1_{catalytic}$, shows a large deformation of the peripheral stalk. **c** The peripheral stalk bends at two pivot points near F_1 (yellow arrow) and near F_O (red arrow). **d** Unstructured regions in subunit h (blue asterisks) allow it to withstand the bending of subunit d.

earlier structures was low due to flexibility in both the peripheral stalk overall and subunit h specifically. Focused refinement of the peripheral stalk in the current structure resulted in continuous density for most of subunit h, allowing for construction of an atomic model for residues 1 to 62 based on predictions from AlphaFold[35] (Fig. 3a, blue; Supplementary Fig. 6). Interestingly, despite density immediately C-terminal of His62 in subunit h appearing disordered, an additional density that interacts with subunits a, d, f, and 8 indicates that the C terminus of the protein reaches the membrane surface, as suggested previously[36] (Fig. 3a, dashed box). Therefore, subunit h spans the entire distance from F_1 to F_O, a role usually attributed only to subunit b, and different from subunit F_6, the shorter mammalian homolog of subunit h[29].

Aligning the eight structures corresponding to State $1_{catalytic}$ by their F_O regions reveals that the dramatic bending of the peripheral stalk is facilitated mainly by deformation of subunits b, d, and h (Fig. 3b; Supplementary Movie 1, 'During ATP hydrolysis' condition). In conformations that show only slight bending of the peripheral stalk, such as State $1_{catalytic}$(b to d),

deviation from the relaxed State $1_{catalytic}$(a) conformation is mediated primarily by a pivot point in subunits b and d close to the membrane surface (Fig. 3c, red arrow). In the more strained conformations like State $1_{catalytic}$(h), a second pivot point in subunit b at the top of subunit d is apparent (Fig. 3c, yellow arrow). The two pivot points are located at either end of subunit d, indicating that subunit d controls where the peripheral stalk bends and likely acts to oppose the bending force, inducing the left-handed curvature of the peripheral stalk when it is not under strain. The structure of subunit d, with an α-helical hairpin that allows it to push against subunit b, is ideal for its role of applying a force that attempts to restore the relaxed conformation of the peripheral stalk during ATP hydrolysis or synthesis (Fig. 3d; Supplementary Movie 1, orange subunit). Subunit h contains two disordered regions close to the two pivot points defined by subunit d, which allows it to withstand the large conformational changes that occurs around the pivot points (Fig. 3d, blue asterisks). In contrast with the spring-like peripheral stalk seen here for the yeast ATP synthase, the unusually large peripheral

stalk of algal ATP synthase from *Polytomella* sp., although imaged in the absence of substrate, appears mostly rigid, with the OSCP subunit that connects the catalytic domain to the rest of the peripheral stalk showing the most flexibility[26].

Overall rotation cycle of yeast ATP synthase. Despite the presence of a high concentration of ATP in the buffer used for freezing specimens during ATP hydrolysis, State $1_{catalytic}$(a), the least strained of the State $1_{catalytic}$ conformations, appears to have MgADP bound in its $\alpha\beta_{tight}$ site (Fig. 4a, left). In contrast, refinement of the F_1 region with particle images combined from State $1_{catalytic}$(e to h), the four most strained of the State $1_{catalytic}$ conformations, resulted in a structure similar to State $1_{catalytic}$(a) but with what appears to be MgATP bound to $\alpha\beta_{tight}$ (Fig. 4a, right). In the presence of free ATP, ATP hydrolysis occurs at the $\alpha\beta_{tight}$ site and MgADP within the site is expected to inhibit this hydrolytic activity. Therefore, the presence of MgADP in $\alpha\beta_{tight}$ of the non-strained conformation suggests that many of the complexes in this conformation are in the well-known MgADP inhibited state[4,37]. Inactive complexes have been detected previously even in the presence of free ATP[38,39]. In contrast, the structures that show the more strained peripheral stalks appear to be calculated from images of active enzyme particles. Density for the binding dwell conformations suggests that they contain MgADP with Pi in the $\alpha\beta_{tight}$ site (Supplementary Fig. 7a), as was seen in the bacterial F_1 region during ATP hydrolysis[32].

To place the 27 conformations of ATP synthase observed during ATP hydrolysis into a rotational sequence, the positions of subunit γ relative to $\alpha_3\beta_3$ in F_1 (Fig. 4b) and of the c-ring relative to subunit a in F_O (Fig. 4c) were measured and plotted on circles that represent a 360° rotation. As described above, the $\alpha_3\beta_3\gamma\delta\epsilon c_{10}$ subcomplex is found in three catalytic dwell conformations and three binding dwell conformations, resulting in only six unique positions of subunit γ relative to $\alpha_3\beta_3$ in F_1 (Fig. 2b). Consistent with the isolated bacterial F_1 region[10,32], ATP hydrolysis in $\alpha\beta_{tight}$ of the yeast catalytic dwell conformation appears to induce a slightly more open conformation of the $\alpha\beta$ pair and a ~36° rotation of the rotor (Supplementary Fig. 7b), leaving the enzyme in a binding dwell. MgADP and Pi are then released from the $\alpha\beta_{tight}$ site and ATP binding to the $\alpha\beta_{open}$ site drives an ~84° rotation of the rotor to the next catalytic dwell conformation. Repetition of this process two more times completes the 360° rotation cycle for ATP hydrolysis (Fig. 4b, clockwise arrows), while for ATP synthesis the reverse reaction is driven by rotation of the rotor in the opposite direction (Fig. 4b, counter-clockwise arrows).

In contrast to the six unique positions of subunit γ relative to $\alpha_3\beta_3$ in F_1, there are 27 unique positions of the c-ring relative to subunit a in F_O. Plotting the angle of the c-ring relative to subunit a in F_O produces a series of arcs that show the range of rotation of the ring within each catalytic or binding dwell state (Fig. 4c, black, blue, yellow, green, red, and cyan arcs). These arcs reveal that as the c-ring rotates in the ATP hydrolysis direction, each state exhibits a decreasing strain on the peripheral stalk (Fig. 4c, clockwise arrow). For example, for State $1_{catalytic}$ (Fig. 4c, black arc), rotation of the c-ring in the ATP hydrolysis direction occurs during the transition from State $1_{catalytic}$(h) → State $1_{catalytic}$(a). As ATP hydrolysis in a catalytic $\alpha\beta_{tight}$ site causes the transition from a catalytic dwell to a binding dwell, the order of states indicates that the power stroke of ATP hydrolysis forces the peripheral stalk into a more strained conformation (e.g., State $1_{catalytic}$(a) → State $1_{binding}$(d)). This strain subsequently relaxes as the c-ring continues to turn in the ATP hydrolysis direction (e.g., State $1_{binding}$(d) → State $1_{binding}$(a)). Conversely, rotation of the c-ring in the direction driven by proton translocation during ATP synthesis (Fig. 4c,

counter-clockwise arrow) leads to increasing strain on the peripheral stalk (e.g., State $1_{binding}$(a) → State $1_{binding}$(d)), which relaxes as ATP is formed in the catalytic site and the enzyme transitions from a binding dwell conformation to a catalytic dwell conformation (e.g., State $1_{binding}$(d) → State $1_{catalytic}$(a)).

Notably, the most strained conformation of some of the states show less rotation of the c-ring in the ATP hydrolysis direction than less strained conformations of the preceding state (Fig. 4c, shaded areas). For example, the transition from State $1_{catalytic}$(a) to State $1_{binding}$(d) during ATP hydrolysis would involve the c-ring rotating 23° in the ATP synthesis direction. The same apparent 'backstepping' can be seen at the transition from State $3_{catalytic}$ → State $3_{binding}$, and State $2_{binding}$ → State $1_{catalytic}$. This backstepping of the c-ring would bend the peripheral stalk in the opposite direction of the applied force and is physically unlikely. Therefore, the unstrained conformations appear to show inactive complexes that are not part of the rotary sequence during substrate turnover. By extension, these data suggest that during rotary catalysis the peripheral stalk becomes strained and does not relax fully until catalysis stops. Construction of a movie showing rotation in the hydrolysis direction based on the most strained conformation of the enzyme illustrates the amount of deformation that can occur during ATP hydrolysis (Supplementary Movie 2, 'ATP hydrolysis' cycle). Similarly, a video can be constructed showing rotation in the ATP synthesis direction based on the most strained conformations (Supplementary Movie 2, 'ATP synthesis' cycle). Together, these data illustrate how in active ATP synthase the peripheral stalk can serve as a buffer for energy that deforms under strain. ATP synthase c-rings from different species can have between eight and 17 c subunits[40] and the flexibility of the peripheral likely allows this variability. The storage of energy during rotation would also be expected to smooth the transmission of power between the F_1 and F_O motors despite symmetry mismatch, which is thought to be essential for the high turnover rate of the enzyme[41,42]. In the fully active enzyme, the peripheral stalk likely remains deformed as the enzyme runs, with the degree of bending dependent on the rate of turnover, and with the enzyme only becoming fully relaxed in the absence of ATP or a proton motive force. At present cryoEM appears uniquely capable of providing high-resolution insight into changes in enzyme conformation that occur during catalysis. Experiments to quantify strain within ATP synthase in solution conditions, such as single-molecule fluorescence resonance energy transfer[43], could complement the findings reported here and reveal how strain changes within individual molecules during each rotation cycle.

Methods

Yeast growth and ATP synthase purification. Yeast strain USY006 containing a 6 × His tag at the N terminus of the β subunits was grown in YPGD media (1% [w/v] yeast extract, 2% [w/v] peptone, 3% [v/v] glycerol, 0.2% [w/v] glucose) with a 11 L fermenter (New Brunswick Scientific) for ~48 h at 30 °C until saturation. All purification steps were performed at 4 °C. Yeast cell walls were broken with bead beating, and cell debris was removed by centrifugation at 5000 × g for 30 min. Mitochondria were collected by centrifugation at 25,000 × g for 30 min, before being washed with phosphate buffer (50 mM sodium phosphate pH 9.0, 5 mM 6-aminocaproic acid, 5 mM benzamidine, 1 mM PMSF) for 30 min. Washed mitochondria were collected by centrifugation at 184,000 × g for 30 min, before being resuspended in buffer (50 mM Tris-HCl pH 7.4, 10% [v/v] glycerol, 1% [w/w] DDM [Anatrace], 5 mM 6-aminocaproic acid, 5 mM benzamidine, 1 mM PMSF) and solubilized with gentle shaking for one hour. Insoluble material was removed by centrifugation at 184,000 × g for 30 min, and supernatant containing solubilized protein was supplemented with 40 mM imidazole and 300 mM NaCl before being loaded onto a 5 mL HisTrap column (Cytiva) equilibrated with HisTrap buffer (50 mM Tris-HCl pH 7.4, 10% [v/v] glycerol, 0.05% [w/w], 40 mM imidazole, 300 mM NaCl, 5 mM 6-aminocaproic acid, 5 mM benzamidine, 1 mM PMSF), and washed with HisTrap buffer. ATP synthase was eluted with HisTrap buffer containing 300 mM imidazole and was loaded onto a Superose 6 Increase column (Cytiva) equilibrated with buffer (20 mM Tris-HCl pH 7.4, 10% [v/v] glycerol, 0.05% [w/w] DDM, 100 mM NaCl, 5 mM
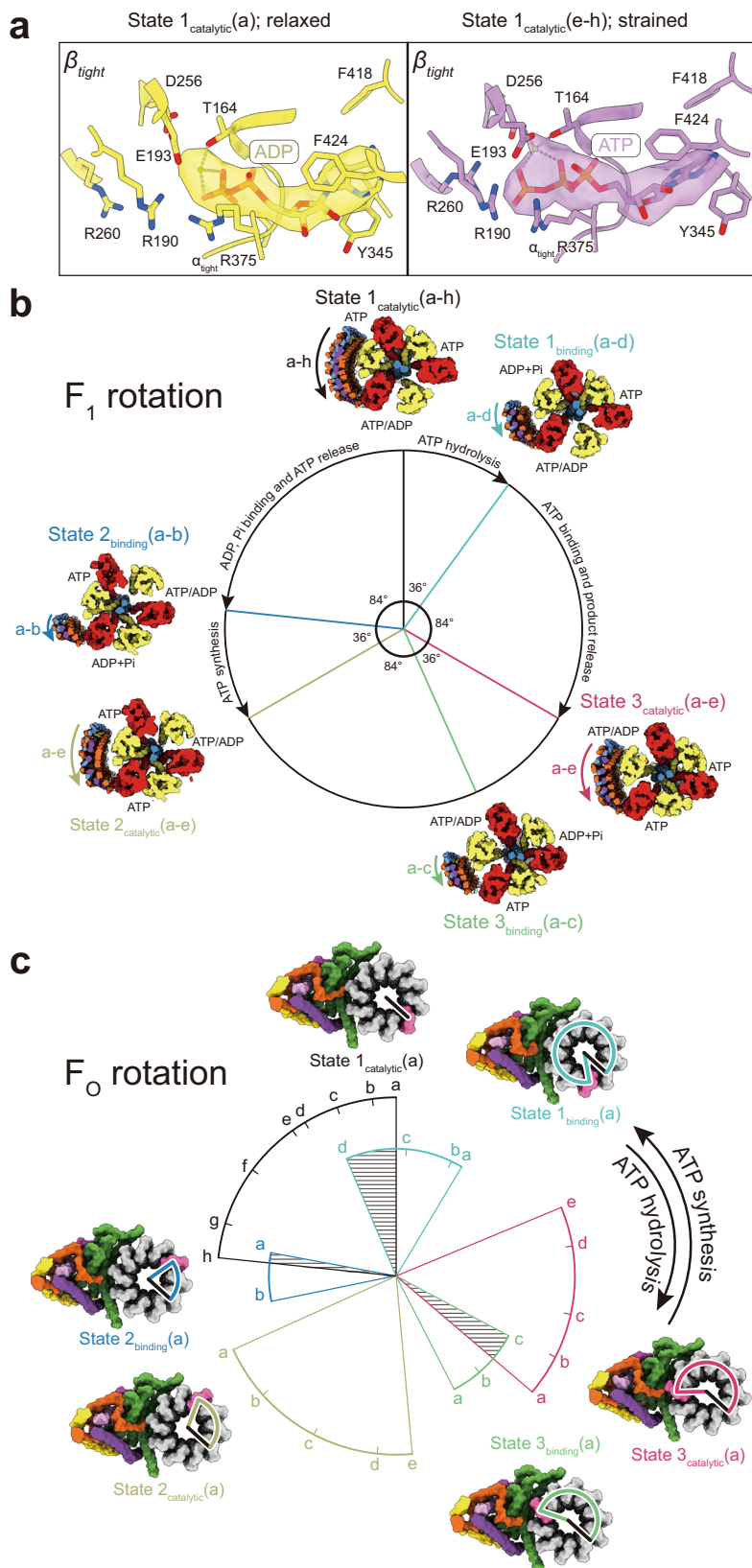
MgCl$_2$). Fractions containing ATP synthase were pooled, and the protein was concentrated to ~15 mg/ml prior to cryoEM grid freezing or storage at −80 °C.

CryoEM specimen preparation. Glycerol in the ATP synthase preparation was removed with a Zeba Spin desalting column (Thermo Fisher Scientific [TFS]) before freezing cryoEM specimens. Holey gold films with ~2 μm holes were

nanofabricated[44] on 300 mesh Maxtaform copper-rhodium grids (Electron Microscopy Sciences). Specimens with 10 mM ATP were prepared by first applying 0.4 μL of 50 mM ATP in buffer (70 mM Tris-HCl pH 7.4, 0.05% [w/w] DDM, 100 mM NaCl, 55 mM MgCl$_2$) onto a grid that had been glow-discharged in air for 2 min. Freshly prepared ATP synthase (1.6 μL) was mixed quickly with the ATP solution on the grid before blotting for 1 s in an EM GP2 grid freezing device

Fig. 4 Sequence of conformations in the ATP hydrolysis and ATP synthesis cycles. a The unstrained conformation of State $1_{catalytic}$ shows density consistent with MgADP in the $\alpha\beta_{tight}$ catalytic pair (left, yellow), suggesting an ADP-inhibited state, while the strained conformations show density consistent with MgATP (right, purple) suggesting an active state. **b** Measurement of the rotation of the rotor subunit γ within the F_1 region shows 36° and 84° sub-steps between catalytic and binding dwell conformations. **c** Measurement of the rotation of the c-ring relative to subunit a in F_O. Within each binding or catalytic dwell conformation the peripheral stalk becomes increasingly strained as the c-ring rotates in the ATP synthesis direction and increasingly relaxed as the c-ring rotates in the ATP hydrolysis direction. Transition between catalytic and binding dwell conformations would require back-stepping of the c-ring (shaded areas) if every conformation occurred during the rotary cycle. Colors in (**b**) and (**c**) are defined as in Fig. 1b.

(Leica) at 4 °C and 100% humidity and plunge frozen in liquid ethane. Specimens without ATP were prepared the same way except that the mixing step was omitted.

CryoEM data collection. Preliminary cryoEM data was collected with FEI Tecnai F20 electron microscope operated at 200 kV and equipped with a Gatan K2 Summit camera. Images with this microscope were acquired as movies with 30 fractions at 5 e/pixel/s and a calibrated pixel size of 1.45 Å/pixel. CryoEM movies for high-resolution analysis were collected with a Titan Krios G3 microscope operated at 300 kV and equipped with a Falcon 4 camera (TFS). Automated data collection was performed with EPU. For the dataset including ATP, 10,037 movies, each consisting of 30 fractions, were collected at a nominal magnification of ×59,000, corresponding to a calibrated pixel size of 1.348 Å. The exposure rate and the total exposure of the specimen were 6.1 e⁻/pixel/s and ~40 e⁻/Å², respectively. For the ATP-free dataset, 8817 30-fraction movies were collected at a nominal magnification of ×75,000, corresponding to a calibrated pixel size of 1.046 Å. The exposure rate and the total exposure for this specimen were 4.2 e/pixel/second and ~39 e/Å², respectively.

Image analysis. Data collection was monitored with cryoSPARC Live[45] to screen and select high-quality micrographs. All other image analysis steps were performed with cryoSPARC except where mentioned. Movie fractions were aligned with patch-based motion correction and contrast transfer function (CTF) parameters were estimated with patch-based CTF estimation. After removing movies with undesirable motion or CTF fit, 7474 and 4059 movies from the dataset including ATP and the ATP-free dataset were selected for further processing, respectively. Movie fractions were aligned with MotionCor[46] with a 7 × 7 grid and averaged micrographs from the aligned movies were subjected to patch-based CTF estimation. For the ATP-free dataset, particle selection was performed with Topaz[47]. For the dataset including ATP, templates for particle selection were generated from 2D classification of manually selected particle images. After particle selection, 2,534,488 particle images were extracted for the dataset with ATP and 442,025 particle images were extracted for the ATP-free dataset. Low-quality particle images were removed with two rounds of 2D classifications, yielding 1,109,677 and 422,765 particle images for the dataset including ATP and the ATP-free dataset, respectively. Further cleaning with ab initio 3D classification and heterogeneous refinement reduced dataset sizes to 915,825 and 379,817 particle images, respectively. The remaining particle images were classified into three classes, corresponding to the three main rotational states of the enzyme, and each class was refined with non-uniform refinement[48]. For the dataset including ATP, local refinement was performed with all particle images with a mask including $\alpha_3\beta_3\gamma\delta\epsilon$ from the F_1 region. CTF parameters of individual particle images were re-estimated with local CTF refinement, and masked refinement was performed again with updated CTF parameters. Image alignment parameters were then converted to Relion[49] .star file format with pyem (https://doi.org/10.5281/zenodo.3576630) and individual particle motion was corrected with Bayesian polishing[50]. For the ATP-free dataset, Bayesian polishing was performed with an intact ATP synthase map reconstructed with all particle images and particle images were down-sampled to a pixel size of 1.308 Å. Motion corrected images were imported back to cryoSPARC, refined, and CTF parameters re-estimated. For the dataset including ATP, particle images were initially classified into four classes. Iterative ab initio classification and heterogeneous refinement of each of the four classes yielded 27 unique rotational states of ATP synthase. The 27 structures were named State $1_{binding}$(a to d), State $1_{catalytic}$(a to h), State $2_{binding}$(a to b), State $2_{catalytic}$(a to e), State $3_{binding}$(a to c), and State $3_{catalytic}$(a to e), and had resolutions ranging from 4.4 to 7.8 Å after refinement. Masked local refinement of the F_1 region of State $1_{catalytic}$(a) yielded a 3.5 Å resolution map representing the MgADP inhibited state. Local refinement of the F_1 region of combined State $1_{catalytic}$(e to h) and State $1_{binding}$(a to d) yielded two 4.0 Å resolution maps. To better visualize the nucleotide density in maps, density modification[51] of locally-refined maps of State $1_{catalytic}$(a), State $1_{catalytic}$(e to h), and State $1_{binding}$(a to d) was performed in Phenix[52]. For the ATP-free dataset, a similar 3D classification strategy yielded nine F_1 states, namely State 1, 2, and $3_{catalytic}$ with $\alpha\beta_{tight}$ in a closed conformation, State 1, 2, and $3_{catalytic}$ with $\alpha\beta_{tight}$ in an open conformation, and State 1, 2, and $3_{binding}$ with $\alpha\beta_{tight}$ in an open conformation (Supplementary Fig. 1 and 3). These states included 56,739, 52,468, 24,879, 31,559, 47,065, 65,651, 19,922, 57,468, and 23,622 particle images, respectively. Local refinement of the F_1 region with these images yielded maps at 3.4, 3.4, 3.6, 3.5, 3.5, 3.4, 3.7, 3.4, and 3.7 Å resolution, respectively. When the three rotational states are combined, the F_1 regions of State$_{catalytic}$ with β_{tight} closed, State$_{catalytic}$ with β_{tight} open, and State$_{catalytic}$ with $\beta_{binding}$ open reached 3.2, 3.2, and 3.3 Å resolution, respectively. Classification of particle images contributing to State $1_{catalytic}$ from the ATP-free dataset yielded 4 classes with different c-ring positions relative to subunit a, which demonstrates the flexibility of the peripheral stalk in the absence of free ATP (Fig. 1d, Supplementary Fig. 1). Maps of these states were calculated from 41,506, 8810, 10,550, and 1984 particle images and reached 3.8, 4.4, 4.4, and 7.1 Å resolutions after refinement, respectively. A similar classification strategy was employed with the other two catalytic states, and particle images of the most relaxed State 1, 2, $3_{catalytic}$(a) (191,939 particle images) were used to calculate locally-refined maps of OSCP with its contact site on F_1, the remainder of the peripheral stalk, and the F_O region. These maps were combined with the map from local refinement of the F_1 region of the State $1_{catalytic}$ with $\alpha\beta_{tight}$ closed using the 'vop maximum' function in USCF Chimera to generate a composite map of the entire complex.

Model building and refinement. To build atomic models of the F_1 region, the crystal structure of yeast F_1 (PDB 2HLD)[53] was fitted as a rigid body into locally-refined maps of F_1 in UCSF Chimera[54]. Models were manually adjusted in Coot[55] before being imported into ISOLDE[56] within ChimeraX[57] to improve dihedral angles and rotamer fitting. A final round of refinement was performed with Phenix and the resulting models were evaluated with Molprobity[58] and EMRinger[59]. To build backbone models of the full complex, a mosaic model was first assembled by rigid-body fitting of a yeast F_1 crystal structure (PDB 2HLD), subunits abc$_{10}$dfi from a yeast F_O cryoEM structure (PDB 6B2Z)[60], the peripheral stalk region without subunit h from a yeast monomer cryoEM structure (PDB 6CP3)[30], and domains of a subunit h atomic model predicted with AlphaFold[35] into the unsharpened maps. Molecular Dynamics Flexible Fitting[61] was then performed for the 27 rotational states of the dataset including ATP to generate corresponding backbone models. Figures and movies were generated with ChimeraX and UCSF Chimera.

Reporting summary. Further information on research design is available in the Nature Research Reporting Summary linked to this article.

Data availability
The data that support this study are available from the corresponding author upon reasonable request. Cryo-EM maps generated in this study have been deposited in the Electron Microscopy Data Bank with accession numbers EMD-25930, EMD-25931, EMD-25932, EMD-25933, EMD-25934, EMD-25935, EMD-25936, EMD-25937, EMD-25938, EMD-25939, EMD-25940, EMD-25941, EMD-25942, EMD-25943, EMD-25944, EMD-25945, EMD-25946, EMD-25947, EMD-25948, EMD-25949, EMD-25950, EMD-25951, EMD-25952, EMD-25953, EMD-25954, EMD-25955, EMD-25956, EMD-25957, EMD-25958, EMD-25959, EMD-25960, EMD-25961, EMD-25962, EMD-25963, EMD-25964, EMD-25965, EMD-25966, EMD-25967, EMD-25968, EMD-25969, EMD-25970, EMD-25971, EMD-25972, EMD-25973, EMD-25974, EMD-25975, EMD-25976, EMD-25977, EMD-25978, EMD-25979, EMD-25980 and atomic models have been deposited in the Protein Data Bank with accession codes 7TJS, 7TJT, 7TJU, 7TJV, 7TJW, 7TJX, 7TJY, 7TJZ, 7TK0, 7TK1, 7TK2, 7TK3, 7TK4, 7TK5, 7TK6, 7TK7, 7TK8, 7TK9, 7TKA, 7TKB, 7TKC, 7TKD, 7TKE, 7TKF, 7TKG, 7TKH, 7TKI, 7TKJ, 7TKK, 7TKL, 7TKM, 7TKN, 7TKO, 7TKP, 7TKQ, 7TKR, 7TKS. Previously published atomic models used for atomic model building are available in the Protein Data Bank with accession codes 2HLD, 6B2Z, 6CP3.

References
1. Junge, W., Lill, H. & Engelbrecht, S. ATP synthase: an electrochemical transducer with rotary mechanics. *Trends Biochem. Sci.* **22**, 420–423 (1997).
2. Vik, S. & Antonio, B. J. A mechanism of proton translocation by F1F0 ATP synthases suggested by double mutants of the a subunit. *J. Biol. Chem.* **269**, 30364–9 (1994).
3. Liu, S. et al. The purification and characterization of ATP synthase complexes from the mitochondria of four fungal species. *Biochem. J.* **468**, 167–175 (2015).
4. Abrahams, J. P., Leslie, A. G. W., Lutter, R. & Walker, J. E. Structure at 2.8 Å resolution of F1-ATPase from bovine heart mitochondria. *Nature* **370**, 621–628 (1994).

5. Bilyard, T. et al. High-resolution single-molecule characterization of the enzymatic states in *Escherichia coli* F1-ATPase. *Philos. Trans. R. Soc. B Biol. Sci.* **368**, 20120023 (2013).

6. Kobayashi, R., Ueno, H., Li, C.-B. & Noji, H. Rotary catalysis of bovine mitochondrial F_1-ATPase studied by single-molecule experiments. *Proc. Natl Acad. Sci. USA* **117**, 1447–1456 (2020).

7. Soga, N., Kimura, K., Kinosita, K., Yoshida, M. & Suzuki, T. Perfect chemomechanical coupling of F_oF_1-ATP synthase. *Proc. Natl Acad. Sci. USA* **114**, 4960–4965 (2017).

8. Stock, D., Leslie, A. G. & Walker, J. E. Molecular architecture of the rotary motor in ATP synthase. *Science* **286**, 1700–1705 (1999).

9. Zhou, A. et al. Structure and conformational states of the bovine mitochondrial ATP synthase by cryo-EM. *eLife* **4**, e10180 (2015).

10. Yasuda, R., Noji, H., Yoshida, M., Kinosita, K. & Itoh, H. Resolution of distinct rotational substeps by submillisecond kinetic analysis of F1-ATPase. *Nature* **410**, 898–904 (2001).

11. Martin, J. L., Ishmukhametov, R., Hornung, T., Ahmad, Z. & Frasch, W. D. Anatomy of F1-ATPase powered rotation. *Proc. Natl Acad. Sci. USA* **111**, 3715–3720 (2014).

12. Steel, B. C. et al. Comparison between single-molecule and X-ray crystallography data on yeast F1-ATPase. *Sci. Rep.* **5**, 8773 (2015).

13. Nishizaka, T. et al. Chemomechanical coupling in F1-ATPase revealed by simultaneous observation of nucleotide kinetics and rotation. *Nat. Struct. Mol. Biol.* **11**, 142–148 (2004).

14. Adachi, K. et al. Coupling of rotation and catalysis in F1-ATPase revealed by single-molecule imaging and manipulation. *Cell* **130**, 309–321 (2007).

15. Cherepanov, D. A., Mulkidjanian, A. Y. & Junge, W. Transient accumulation of elastic energy in proton translocating ATP synthase. *FEBS Lett.* **449**, 1–6 (1999).

16. Pänke, O. & Rumberg, B. Kinetic modeling of rotary CF0F1-ATP synthase: storage of elastic energy during energy transduction. *Biochim. Biophys. Acta BBA - Bioenerg.* **1412**, 118–128 (1999).

17. Lau, W. C. Y., Baker, L. A. & Rubinstein, J. L. Cryo-EM structure of the yeast ATP synthase. *J. Mol. Biol.* **382**, 1256–1264 (2008).

18. Rubinstein, J. L., Walker, J. E. & Henderson, R. Structure of the mitochondrial ATP synthase by electron cryomicroscopy. *EMBO J.* **22**, 6182–6192 (2003).

19. Flygaard, R. K., Mühleip, A., Tobiasson, V. & Amunts, A. Type III ATP synthase is a symmetry-deviated dimer that induces membrane curvature through tetramerization. *Nat. Commun.* **11**, 5342 (2020).

20. Gu, J. et al. Cryo-EM structure of the mammalian ATP synthase tetramer bound with inhibitory protein IF1. *Science* **364**, 1068–1075 (2019).

21. Guo, H., Suzuki, T. & Rubinstein, J. L. Structure of a bacterial ATP synthase. *eLife* **8**, e43128 (2019).

22. Hahn, A., Vonck, J., Mills, D. J., Meier, T. & Kühlbrandt, W. Structure, mechanism, and regulation of the chloroplast ATP synthase. *Science* **360**, eaat4318 (2018).

23. Hahn, A. et al. Structure of a complete ATP synthase dimer reveals the molecular basis of inner mitochondrial membrane morphology. *Mol. Cell* **63**, 445–456 (2016).

24. Mühleip, A. et al. ATP synthase hexamer assemblies shape cristae of *Toxoplasma* mitochondria. *Nat. Commun.* **12**, 120 (2021).

25. Mühleip, A., McComas, S. E. & Amunts, A. Structure of a mitochondrial ATP synthase with bound native cardiolipin. *eLife* **8**, e51179 (2019).

26. Murphy, B. J. et al. Rotary substates of mitochondrial ATP synthase reveal the basis of flexible F1-Fo. *Science* **364**, eaaw9128 (2019).

27. Pinke, G., Zhou, L. & Sazanov, L. A. Cryo-EM structure of the entire mammalian F-type ATP synthase. *Nat. Struct. Mol. Biol.* **27**, 1077–1085 (2020).

28. Sobti, M. et al. Cryo-EM structures of the autoinhibited *E. coli* ATP synthase in three rotational states. *eLife* **5**, e21598 (2016).

29. Spikes, T. E., Montgomery, M. G. & Walker, J. E. Structure of the dimeric ATP synthase from bovine mitochondria. *Proc. Natl Acad. Sci. USA* **117**, 23519–23526 (2020).

30. Srivastava, A. P. et al. High-resolution cryo-EM analysis of the yeast ATP synthase in a lipid membrane. *Science* **360**, eaas9699 (2018).

31. Rubinstein, J. L. & Walker, J. E. ATP synthase from *Saccharomyces cerevisiae*: location of the OSCP subunit in the peripheral stalk region. *J. Mol. Biol.* **321**, 613–619 (2002).

32. Sobti, M., Ueno, H., Noji, H. & Stewart, A. G. The six steps of the complete F1-ATPase rotary catalytic cycle. *Nat. Commun.* **12**, 4690 (2021).

33. Sorgen, P. L., Bubb, M. R. & Cain, B. D. Lengthening the second stalk of F1F0 ATP synthase in *Escherichia coli*. *J. Biol. Chem.* **274**, 36261–36266 (1999).

34. Sorgen, P. L., Caviston, T. L., Perry, R. C. & Cain, B. D. Deletions in the second stalk of F1F0-ATP synthase in *Escherichia coli*. *J. Biol. Chem.* **273**, 27873–27878 (1998).

35. Jumper, J. et al. Highly accurate protein structure prediction with AlphaFold. *Nature* **596**, 583–589 (2021).

36. Rubinstein, J. L., Dickson, V. K., Runswick, M. J. & Walker, J. E. ATP synthase from *Saccharomyces cerevisiae*: location of subunit h in the peripheral stalk region. *J. Mol. Biol.* **345**, 513–520 (2005).

37. Bowler, M. W., Montgomery, M. G., Leslie, A. G. W. & Walker, J. E. Ground state structure of F1-ATPase from bovine heart mitochondria at 1.9 Å resolution. *J. Biol. Chem.* **282**, 14238–14242 (2007).

38. Hirono-Hara, Y. et al. Pause and rotation of F1-ATPase during catalysis. *Proc. Natl Acad. Sci. USA* **98**, 13649–13654 (2001).

39. Noji, H., Yasuda, R., Yoshida, M. & Kinosita, K. Jr. Direct observation of the rotation of F1-ATPase. *Nature* **386**, 299–302 (1997).

40. Kuhlbrandt, W. Structure and mechanisms of F-type ATP synthases. *Annu. Rev. Biochem.* **88**, 515–549 (2019).

41. Junge, W., Sielaff, H. & Engelbrecht, S. Torque generation and elastic power transmission in the rotary F_OF_1-ATPase. *Nature* **459**, 364–370 (2009).

42. Junge, W. et al. Inter-subunit rotation and elastic power transmission in F0F1-ATPase. *FEBS Lett.* **504**, 152–160 (2001).

43. Börsch, M. & Duncan, T. M. Spotlighting motors and controls of single F_OF_1-ATP synthase. *Biochem. Soc. Trans.* **41**, 1219–1226 (2013).

44. Marr, C. R., Benlekbir, S. & Rubinstein, J. L. Fabrication of carbon films with approximately 500 nm holes for cryo-EM with a direct detector device. *J. Struct. Biol.* **185**, 42–47 (2014).

45. Punjani, A., Rubinstein, J. L., Fleet, D. J. & Brubaker, M. A. cryoSPARC: algorithms for rapid unsupervised cryo-EM structure determination. *Nat. Methods* **14**, 290–296 (2017).

46. Zheng, S. Q. et al. MotionCor2: anisotropic correction of beam-induced motion for improved cryo-electron microscopy. *Nat. Methods* **14**, 331–332 (2017).

47. Bepler, T. et al. Positive-unlabeled convolutional neural networks for particle picking in cryo-electron micrographs. *Nat. Methods* **16**, 1153–1160 (2019).

48. Punjani, A., Zhang, H. & Fleet, D. J. Non-uniform refinement: adaptive regularization improves single-particle cryo-EM reconstruction. *Nat. Methods* **17**, 1214–1221 (2020).

49. Scheres, S. H. W. RELION: implementation of a Bayesian approach to cryo-EM structure determination. *J. Struct. Biol.* **180**, 519–530 (2012).

50. Zivanov, J., Nakane, T. & Scheres, S. H. W. A Bayesian approach to beam-induced motion correction in cryo-EM single-particle analysis. *IUCrJ* **6**, 5–17 (2019).

51. Terwilliger, T. C., Ludtke, S. J., Read, R. J., Adams, P. D. & Afonine, P. V. Improvement of cryo-EM maps by density modification. *Nat. Methods* **17**, 923–927 (2020).

52. Adams, P. D. et al. PHENIX: a comprehensive Python-based system for macromolecular structure solution. *Acta Crystallogr. D. Biol. Crystallogr.* **66**, 213–221 (2010).

53. Kabaleeswaran, V., Puri, N., Walker, J. E., Leslie, A. G. W. & Mueller, D. M. Novel features of the rotary catalytic mechanism revealed in the structure of yeast F1 ATPase. *EMBO J.* **25**, 5433–5442 (2006).

54. Pettersen, E. F. et al. UCSF Chimera—a visualization system for exploratory research and analysis. *J. Comput. Chem.* **25**, 1605–1612 (2004).

55. Emsley, P. & Cowtan, K. Coot: model-building tools for molecular graphics. *Acta Crystallogr. D. Biol. Crystallogr.* **60**, 2126–2132 (2004).

56. Croll, T. I. ISOLDE: a physically realistic environment for model building into low-resolution electron-density maps. *Acta Crystallogr. Sect. Struct. Biol.* **74**, 519–530 (2018).

57. Goddard, T. D. et al. UCSF ChimeraX: meeting modern challenges in visualization and analysis. *Protein Sci.* **27**, 14–25 (2018).

58. Chen, V. B. et al. MolProbity: all-atom structure validation for macromolecular crystallography. *Acta Crystallogr. D. Biol. Crystallogr.* **66**, 12–21 (2010).

59. Barad, B. A. et al. EMRinger: side chain–directed model and map validation for 3D cryo-electron microscopy. *Nat. Methods* **12**, 943–946 (2015).

60. Guo, H., Bueler, S. A. & Rubinstein, J. L. Atomic model for the dimeric FO region of mitochondrial ATP synthase. *Science* **358**, 936–940 (2017).

61. Trabuco, L. G., Villa, E., Mitra, K., Frank, J. & Schulten, K. Flexible fitting of atomic structures into electron microscopy maps using molecular dynamics. *Structure* **16**, 673–683 (2008).

Acknowledgements

Author contributions

J.L.R. conceived the project and supervised the research. H.G. purified the protein, performed the cryoEM, image analysis, and atomic model building. H.G. and J.L.R. wrote the manuscript and prepared figures.

Competing interests

The authors declare no competing interests.

Additional information

Supplementary information The online version contains supplementary material available at https://doi.org/10.1038/s41467-022-29893-2.

Correspondence and requests for materials should be addressed to John L. Rubinstein.

Peer review information *Nature Communications* thanks the anonymous reviewers for their contribution to the peer review of this work. Peer reviewer reports are available.

Reprints and permission information is available at http://www.nature.com/reprints

Publisher's note Springer Nature remains neutral with regard to jurisdictional claims in published maps and institutional affiliations.